metals

MDPI

Article

Microstructure and Mechanical Properties of Ti-6Al-4V In Situ Alloyed with 3 wt% Cr by Laser Powder Bed Fusion

Valerie Sue Goettgens [1,*], Luca Weber [1], Jakob Braun [1], Lukas Kaserer [1], Ilse Letofsky-Papst [2], Stefan Mitsche [2], David Schimbäck [3] and Gerhard Leichtfried [1]

[1] Faculty of Engineering Sciences, Department of Mechatronics, Materials Science, University of Innsbruck, Innrain 52, 6020 Innsbruck, Austria; luca.weber@student.uibk.ac.at (L.W.); jakob.braun@uibk.ac.at (J.B.); lukas.kaserer@uibk.ac.at (L.K.); gerhard.leichtfried@uibk.ac.at (G.L.)

[2] Institute for Electron Microscopy and Nanoanalysis and Center for Electron Microscopy, Graz University of Technology, NAWI Graz, Steyrergasse 17, 8010 Graz, Austria; ilse.papst@tugraz.at (I.L.-P.); stefan.mitsche@felmi-zfe.at (S.M.)

[3] Airbus Central R & T, Airbus Defence and Space GmbH, 82024 Taufkirchen, Germany; david-erich.schimbaeck@airbus.com

* Correspondence: valerie.goettgens@uibk.ac.at

Abstract: This work studied the microstructure and mechanical properties of Ti-6Al-4V in situ alloyed with 3 wt% Cr by laser powder bed fusion (LPBF). Specimens with a relative density of 99.14 ± 0.11% were produced, showing keyhole and lack of fusion pores. Due to incomplete mixing of the components during melting, chemical inhomogeneities were observed in the solidified material. The addition of Cr promoted thermal supercooling during solidification and induced a reduction in the primary β grain size in the longitudinal direction and a weakening of the otherwise strong $\langle 100 \rangle_\beta$ texture, both typical issues for Ti-6Al-4V produced by LPBF. The primary β at first transformed martensitically to α′, but by preheating the substrate plate to 500 °C and cyclically reheating the material by melting subsequent layers, in situ martensite decomposition was achieved, resulting in a fine lamellar α + β microstructure. In addition, the B19 phase was detected in the β matrix, presumably caused by Fe impurities in the Cr powder feedstock. Specimens exhibited a hardness of 402 ± 18 HV_{10}, and an excellent ultimate tensile strength of 1450 ± 22 MPa at an elongation at break of 4.5 ± 0.2%.

Keywords: titanium alloys; laser powder bed fusion; additive manufacturing; alloy development

check for updates

Citation: Goettgens, V.S.; Weber, L.; Braun, J.; Kaserer, L.; Letofsky-Papst, I.; Mitsche, S.; Schimbäck, D.; Leichtfried, G. Microstructure and Mechanical Properties of Ti-6Al-4V In Situ Alloyed with 3 wt% Cr by Laser Powder Bed Fusion. *Metals* **2024**, *14*, 715. https://doi.org/10.3390/met14060715

Received: 10 May 2024
Revised: 5 June 2024
Accepted: 14 June 2024
Published: 16 June 2024

Copyright: © 2024 by the authors. Licensee MDPI, Basel, Switzerland. This article is an open access article distributed under the terms and conditions of the Creative Commons Attribution (CC BY) license (https://creativecommons.org/licenses/by/4.0/).

1. Introduction

Laser powder bed fusion (LPBF), the most widely used additive manufacturing technology for metals and alloys, uses a high-energy laser to fuse powder particles layer by layer [1]. The extremely high cooling rate of up to 10^8 K/s occurring in this process [2] typically induces martensite formation in Ti-6Al-4V, the most commonly used Ti alloy in LPBF [3]. Martensite (α′) is generally undesirable, as it causes severe embrittlement [4–6]. It is a common practice for Ti-6Al-4V LPBF parts to be heat-treated after the process to achieve the transformation of α′ into a stable α + β microstructure. As a result, the ductility of the material is improved at the expense of tensile strength [7,8]. Only in very few studies lamellar α + β was obtained via in situ martensite decomposition in LPBF [3,9].

Besides Ti-6Al-4V, it's modifications are increasingly studied in LPBF. For this purpose, in situ alloying is often applied. LPBF in situ alloying is a commonly used research technique, in which elemental or alloy components are mixed and subsequently fabricated. It is a cost-effective and rapid approach to explore novel alloy compositions, but it also has drawbacks such as incomplete mixing and a high level of defects. The latter are associated to the quite different thermophysical properties of the alloy components [10]. In the field of titanium alloys in general, various alloy additions have been investigated such as Mo [11],

Nb [11–14] Ni [15], Ta [11], Re [16], Fe [17], Cu [18–20], and Cr [11]. Interesting results were obtained, especially in terms of mechanical properties and microstructural features. In situ alloying was used, for example, by Vrancken et al. [21] to investigate the effect of adding 10 wt% Mo to Ti-6Al-4V ELI. They observed a microstructure, consisting predominantly of β instead of the typical α′ in Ti-6Al-4V. The specimens showed an elongation of 20%, which is much higher compared to Ti-6Al-4V ELI with an elongation of 7%. Zhang et al. [22] fabricated Ti-6Al-4V alloyed with up to 6 wt% 316 L stainless steel and reported a modulated α′ + β microstructure, a high tensile strength, and an excellent work-hardening capacity. The studies of Nagase et al. [11] revealed that the addition of 20 at% Cr led to a complete stabilization of β, showing a strong $\langle 100 \rangle_\beta$ texture. A mechanical characterization was not performed. In one of our own studies, Ti-6Al-4V alloyed with 3.5 wt% Cu has been investigated, showing increased tensile strength, an in situ martensite decomposition, and the precipitation of Ti_2Cu [23]. In our own study and in the studies of Vrancken et al. [21], Zhang et al. [22], and Nagase et al. [11], the alloying elements added to Ti-6Al-4V were Cu, Mo, mainly Fe in the case of 316 L, and Cr. These alloying constituents are β-stabilizing elements which, depending on their concentration, can cause the presence of either stable or metastable β [24]. While Mo is an isomorphous β-stabilizer showing a monotectoid reaction, Cu, Fe, and Cr are eutectoid alloying elements [24]. They are characterized by the eutectoid reaction $\beta \longrightarrow \alpha + Ti_xA_Y$ with Ti_xA_Y as an intermetallic compound that can be used as a strengthening effect [25]. For this reason and their effect on β-stability, eutectoid β-stabilizers are considered to be a particularly interesting and versatile class of alloying elements to be investigated.

In general, the use of Cr as an alloying element in titanium alloys is a versatile and interesting additive for several reasons. For example, Cr enhances the corrosion resistance of Ti alloys by promoting the formation of a protective oxide layer [26]. Furthermore, in binary Ti-Cr alloys, the elastic modulus and the hardness increase with a higher Cr content, which is assumed to be due the formation of ω [27,28]. Possible hardening can also occur by the precipitation of $TiCr_2$, following the eutectoid reaction [26]. It has also been found that in cast Ti-Cr alloys, Cr can induce grain refinement via constitutional supercooling [29]. In the context of LPBF, the addition of Cr is of particular interest, as it has the potential to improve alloy performance, which is demonstrated in this work. For this purpose, Ti-6Al-4V in situ alloyed with 3 wt% Cr is investigated with respect to the effect on microstructure evolution, solidification behavior, and mechanical properties. For comparability, the addition of 3 wt% Cr is approximately equivalent to 3.5 wt% Cu in Ti-6Al-4V calculated in at%, which was fabricated in previous studies [23]. Similar to Ti-6Al-4V with 3.5 wt% Cu, martensite decomposition is successfully achieved in this study. This is considered advantageous in terms of ductility, counteracting the strengthening mechanisms achieved by Cr, some of which are accompanied by embrittlement. Thus, excellent tensile strength at moderate elongation is demonstrated. It is shown that the thermal undercooling effect of Cr can be used to avoid coarse columnar grain growth and the strong $\langle 100 \rangle_\beta$ texture which is a typical issue of Ti-6Al-4V, resulting in a more isotropic microstructure. In addition, the occurrence of the B19 phase in this alloy system is reported for the first time.

2. Materials and Methods

Spherical powders of Ti-6Al-4V (15–45 µm, ECKART TLS GmbH, Bitterfeld-Wolfen, Germany) and 3 wt% Cr (45–63 µm, chemPUR GmbH, Karlsruhe, Germany) were mixed in a 3D shaker (Turbula T2 F mixer) for 1 h. The chemical composition of the powders was determined by inductively coupled plasma optical emission spectrometry (ICP-OES), combustion analysis, and inert gas fusion. ICP-OES was also used to assess the chemical composition of the LPBF manufactured specimens. The tap and the bulk density of the powder blend were determined according to DIN EN ISO 3923-1 and DIN EN ISO 3953, respectively, using a Landgraf Laborsysteme device. The flowability of the powder was determined by ISO 4490:2018. An AconityMIDI (Aconity GmbH, Herzogenrath, Germany)

equipped with a 400 W Yb:YAG fibre laser (1064 nm) was used for the LPBF experiments. High-purity argon (≥99.99%) was used as the process gas to achieve an oxygen content <100 ppmv in the build chamber. The substrate plate was preheated to 500 °C. A cuboid specimen (12 × 12 × 12 mm) and four cylindrical specimens with a diameter of 10 mm were fabricated for the tensile specimens. For all specimens, a stripe scanning strategy was used with a stripe width of 5 mm and a zig zag pattern. The scanning direction was rotated by 67° in each layer. The scanning speed, hatch distance, layer thickness, and focus diameter are given in Table 1, which have been optimised on the basis of relative density (RD) maximisation. The RD of the cuboid specimens was determined by the Archimedean principle using distilled water at 20 °C. The referring theoretical density (TD) was calculated with ThermoCalc 2023a [30] and the TCS Ti/TiAl-based alloys database. The cylindrical specimens were fabricated in a perpendicular orientation to the building direction with volume support structures and were machined to the final geometry of the tensile specimens. Tensile tests were performed on four specimens according to EN ISO 6892-1 at room temperature. The Vickers hardness of the material was determined by five indents distributed over the cross section of the specimen with an EMCO Test M1C010 (EMCO GmbH, Kuchl, Austria) at a load of 98.07 N. For tensile properties and Vickers hardness, means and standard deviations were calculated.

Table 1. LPBF process parameters.

Power (W)	Scanning Speed (mm/s)	Hatch Distance (µm)	Layer Thickness (µm)	Focus Diameter (µm)
280	1000	140	45	80

X-ray diffraction (XRD) analysis was performed on the on the cuboid specimen using an Empyrean Panalytical (Malvern Panalytical Ltd., Malvern, UK) in the Bragg–Brentano configuration with Cu $K_{\alpha 1}$ radiation, V = 40 V, I = 20 mA, and a step size of 0.013°. For the cuboid specimen, the top layer, representing the last melted layer, and the cross section of the specimen were measured. The cross section corresponds to the entire material produced. Le Bail analysis (Bruker TOPAS 2.12 software) was used to determine the lattice parameters of α and α′ in the obtained XRD patterns for their differentiation.

A metallographic cross section of the cuboid specimen was prepared by grinding and polishing with an orientation in the building direction (BD) for optical microscopy (OM), scanning electron microscopy (SEM), and electron backscatter diffraction (EBSD) measurements. OM was carried out using a VHX-7000N (Keyence, Kansas City, MO, USA). SEM was conducted on Axia ChemiSEM (FisherScientific, Hampton, IA, USA) in backscatter electron (BSE) mode. EBSD measurements were performed using a Zeiss Ultra 55 SEM equipped with a Thorlabs Fast Frame Rate Scientific camera and OIM DC V7.3.1 software. An acceleration voltage of 12 kV and a beam current of 6.6 nA were used for all investigations. The image sizes were 1000 × 1000 µm and 500 × 500 µm, measured with a step size of 0.5 µm for both scan areas. Energy dispersive X-ray spectroscopy (EDS) images of Ti, Al, V, Cr, and Fe were simultaneously recorded. From the EBSD data, inverse pole figure (IPF) maps were calculated for the BD. For the IPF and phase maps, only grains consisting of at least two adjacent, clearly identified measurement points were considered. The primary β crystallographic texture was reconstructed using MTEX 5.10.0 software according to the Burgers Orientation Relationship (BOR) $(0001)_\alpha // (100)_\beta$ and $\langle 111 \rangle_\beta // \langle 11\bar{2}0 \rangle$ [2]. A probe-corrected FEI TITAN 3 G2 at 300 kV in scanning transmission electron microscopy (STEM) mode was used for microstructural analysis at the nanometer scale to obtain high-angle annular dark-field (HAADF) and annular dark-field (ADF) images. Fast Fourier transformation (FFT) of the HAADF and ADF images was used for phase identification. The specimen was prepared for STEM examination using the FEI FIB Nanolab 200. The data analysis was carried out using DigitalMicrograph 3.52.3932.0 Software (Gatan, Pleasanton, CA, USA). For EDS in STEM investigations, the microscope

was equipped with a windowless silicon drift detector Super-X (Chemi-STEM technology, Thermo FisherScientific, Waltham, MA, USA).

Thermodynamic calculations were performed with ThermoCalc 2023a [30] with the TCS Ti/TiAl-based alloys database.

3. Results

3.1. Rheological Powder Properties and Part Density

The bulk and the tap density, the powder flowability, the Carr index, and the Hausner ratio of the powder blend are listed in Table 2.

Table 2. Powder properties of the Ti-6Al-4V–3Cr powder mixture.

Material	Bulk Density (g/cm^3)	Tap Density (g/cm^3)	Flowability	Carr Index	Hausner Ratio
Ti-6Al-4V–3Cr	2.47 ± 0.02	2.9 ± 0.2	2.4 ± 0.05 g/s	0.15	1.17

The RD of the specimens was 99.14 ± 0.11%. The OM image in Figure 1a shows an overview of the porosity of the specimen. At higher magnification, spherical keyhole pores can be seen in Figure 1b and irregularly shaped lack-of-fusion pores in Figure 1c.

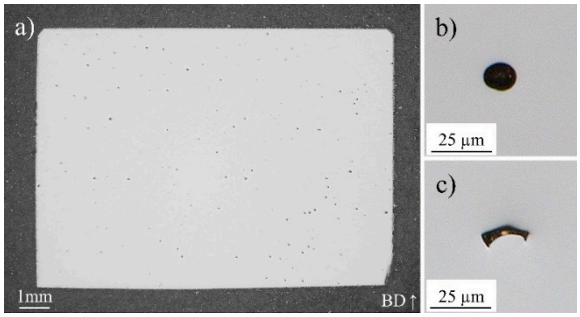


Figure 1. OM image of the sample (**a**) showing keyhole (**b**) and lack of fusion porosity (**c**).

3.2. Chemical Composition

The chemical composition of the Ti-6Al-4V and Cr powders in wt% and the LPBF specimen are given in Table 3.

Table 3. Chemical composition of the powders and the LPBF specimen in wt%.

Ti-6Al-4V Powder (wt%)							
Ti	Al	V	Fe	H	C	N	O
Balance	6.16	4.08	0.18	0.001	0.012	0.05	0.13
Cr powder (wt%)							
Cr		Fe	Al		Si	C	
Balance		0.12	0.01		0.03	0.0037	
Ti-6Al-4V–3Cr specimen (wt%)							
Ti	Al	V	Cr	Fe	C	N	O
Balance	5.9	4.2	1.67	0.17	0.01	0.02	0.15

3.3. XRD

The XRD measurements show that α′ is predominant in the top layer, while β is present to a smaller extent (Figure 2). The lattice parameter ratio c/a for α′ in the top layer is 1.587, suggesting a martensitic state [3]. At an angle of 2θ = 19.5°, a low intensity

peak is observed. This may indicate the presence of B19. In the XRD measurement of the cross section, mainly α and β are found. Here, the β shows a more pronounced peak compared to the top layer. The α is identified by the c/a ratio of 1.597, showing it to be non-martensitic [3]. As in the top layer, a low intensity peak of B19 is indicated. The lattice parameters and lattice parameter ratios c/a of α and α′ are given in Table 4.

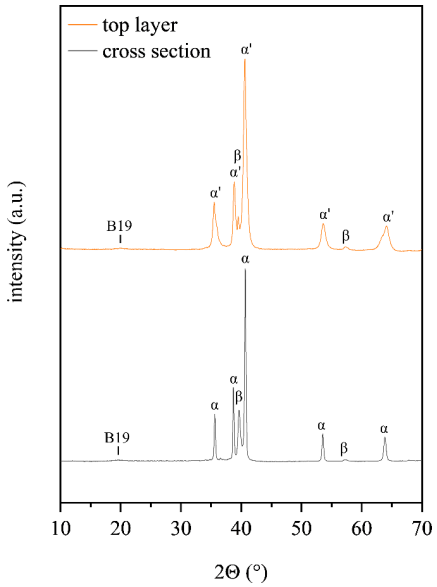


Figure 2. XRD pattern of the top layer and the cross section of the LPBF specimen.

Table 4. Lattice parameters of α and α′.

Sampling Location	Lattice Parameters of α/α′ (Å)	Lattice Parameter Ratio c/a
Top layer	a = 2.918, c = 4.631	1.587
Cross section	a = 2.913, c = 4.652	1.597

3.4. SEM

Figure 3a shows an SEM BSE image of an area of the sample where the Cr and Ti-6Al-4V powder mixture was not adequately homogenized by in situ alloying during LPBF. Cr-rich areas appear brighter due to the Z-contrast. Figure 3b shows a fine-grained lamellar microstructure with a brighter matrix. Based on the Z-contrast, the brighter matrix is likely to be enriched in of V, Cr, and Fe, suggesting β. An α continuous grain boundary (αGB) is present.

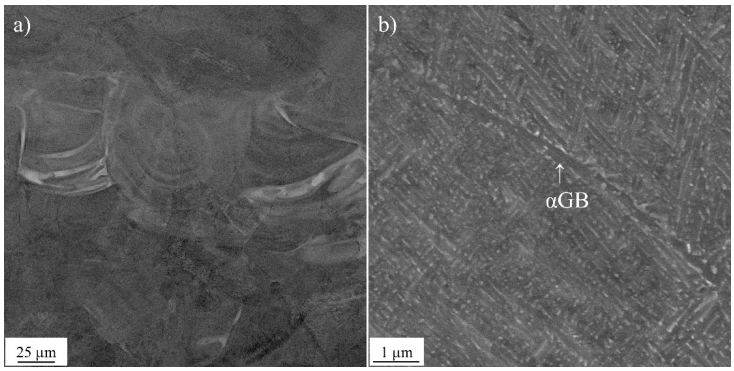


Figure 3. SEM BSE images of the LPBF specimen center. (**a**) Inhomogeneous Cr distribution in the alloy. (**b**) Lamellar α + β microstructure with an αGB.

3.5. EBSD

Figure 4a shows an EBSD phase map with α and β in the BD. The material contains a substantial amount of fine-grained, lamellar α, and fewer lenticular β inclusions. The latter correlate with Cr measured by simultaneous EDS analysis (Figure 4b). Figure 4c shows an IPF map of α, demonstrating its small grain size. Elongated α is almost not visible. In Figure 4d, the reconstructed IPF map of primary β by applying the BOR reveals a non-columnar grain growth. In the areas that remain black in Figure 4a,c, the EBSD signal was unidentifiable. This is suspected to be due to a grain size below the resolution limit or distorted crystal lattices. Figure 5a is an IPF map of the reconstructed primary β of a larger area used for texture determination. No columnar grain growth is seen here either. Primary β shows a slightly pronounced $\langle 111 \rangle_\beta$ texture along the BD, reflected in the IPFs in Figure 5b.

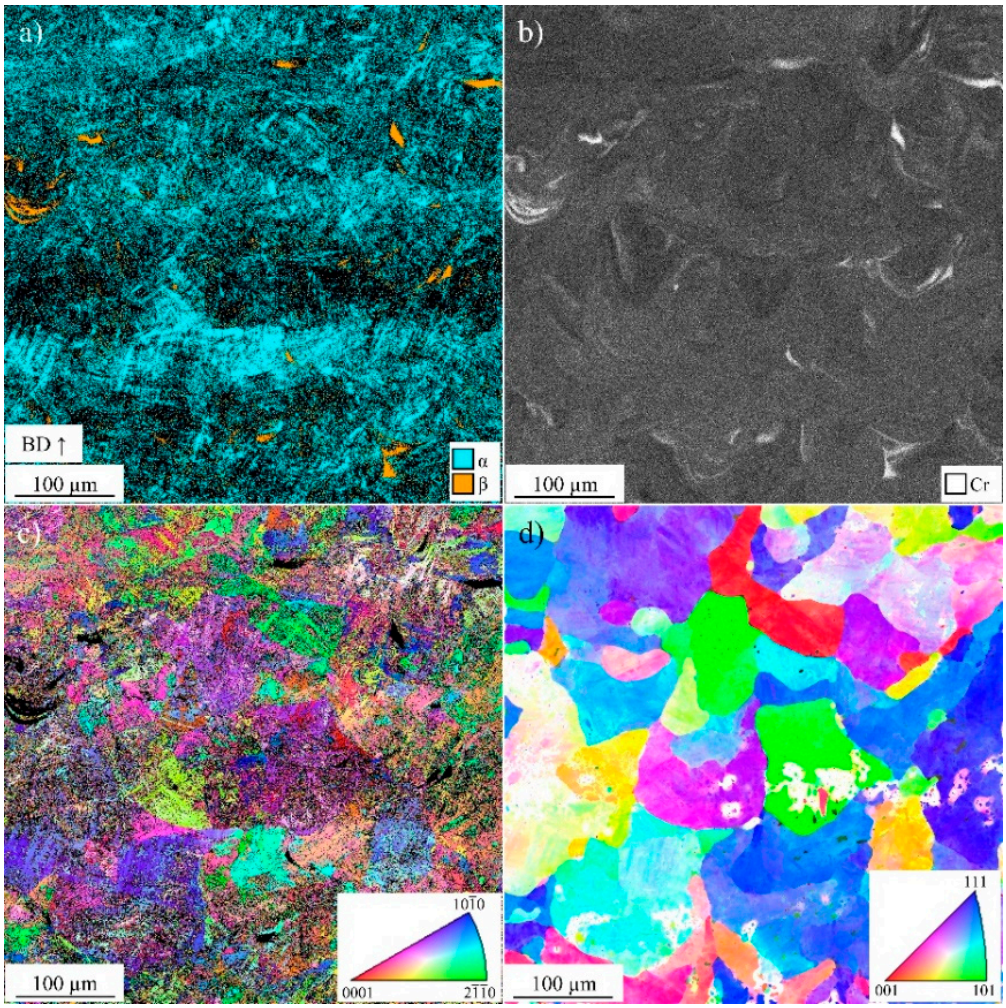


Figure 4. (**a**) EBSD phase map in the BD. (**b**) Simultaneously recorded EDS map. (**c**) IPF map of α. (**d**) Reconstructed phase map of primary β.

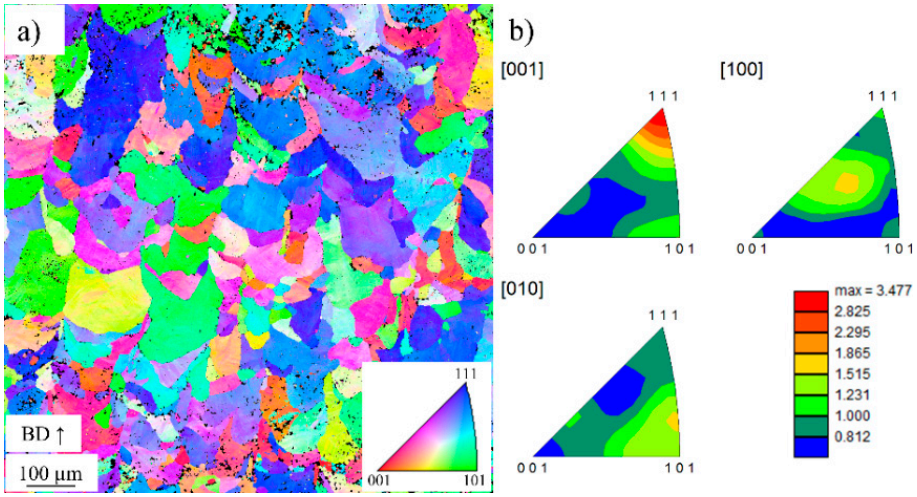


Figure 5. (**a**) Reconstructed IPF map of primary β in the BD. (**b**) Referring inverse pole figures in [001] corresponding to the BD, [100], and [010].

3.6. STEM

Figure 6a shows an HAADF image with elongated grains in a lighter matrix. Areas A and B are highlighted and magnified in Figures 7a and 8a. In Figure 6b–f, EDS mappings of Ti, Al, V, Fe, and Cr are shown. The lighter matrix in Figure 6a shows a higher proportion of V, Fe, and Cr, but a depletion of Al. EDS was used to determine the chemical composition of several regions (ROI 1–3 in Figure 6f). ROI 1 is located in area A and includes only matrix material, containing the highest amount of V, Fe, and Cr (Table 5). ROI 2 is in area B and contains matrix material as well. Compared to ROI 1, ROI 2 has a lower percentage of V, Fe, and Cr (Table 5). ROI 3 is positioned in an elongated grain and contains the lowest amount of V, Fe, and Cr (Table 5).

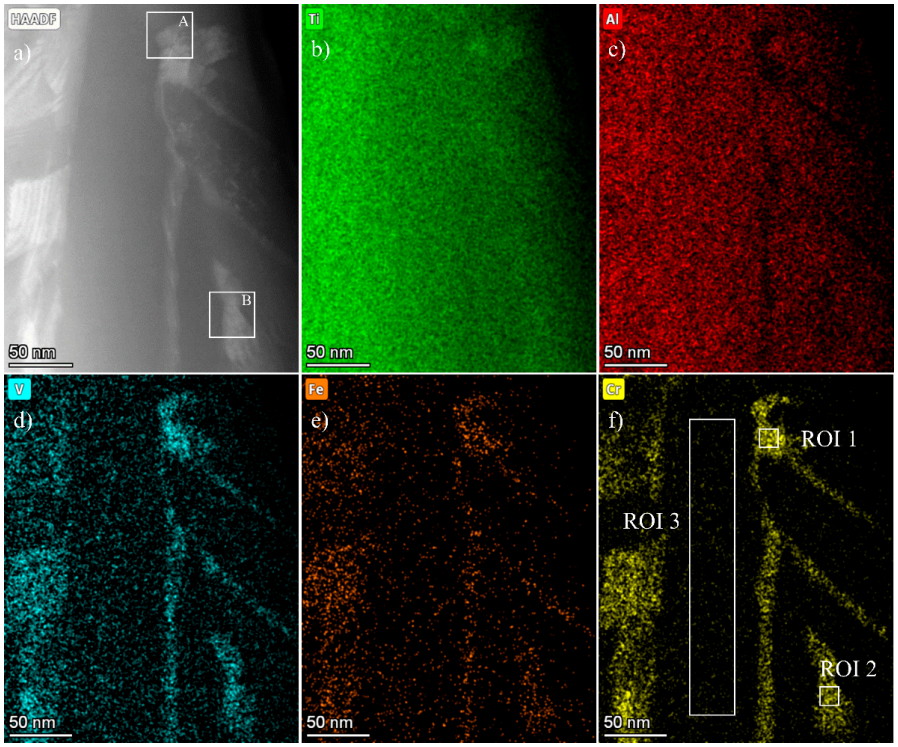


Figure 6. (**a**) STEM HAADF with area A and B. (**b**–**f**) EDS maps for Ti, Al, V, Fe, and Cr. In (**f**), ROI 1–3 are marked.

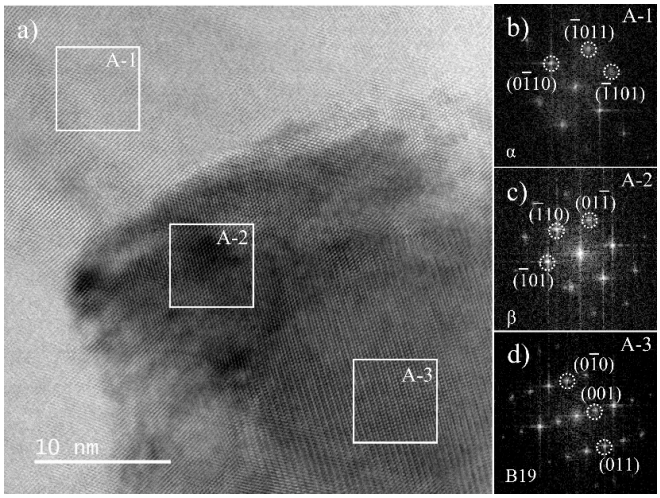


Figure 7. (**a**) ADF of area A (see Figure 6a) with areas A-1, A-2, and A-3. (**b**) FFT of A-1 with α. (**c**) FFT of A-2 with β. (**d**) FFT of A-3 with B19.

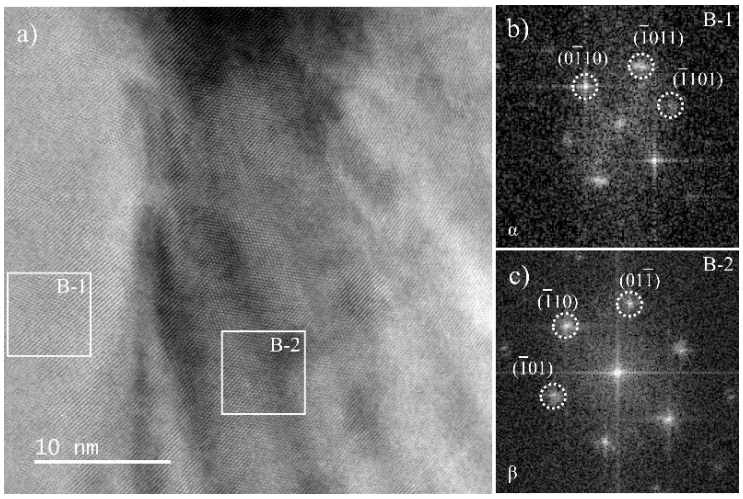


Figure 8. (**a**) ADF of area B (see Figure 6a) with areas B-1 and B-2. (**b**) FFT of B-1 with α. (**c**) FFT of B-2 with β.

Table 5. Chemical compositions of ROI 1–3 in d.

Area	Ti (at%)	Al (at%)	V (at%)	Cr (at%)	Fe (at%)
ROI 1	66.82 ± 4.16	4.06 ± 0.54	16.88 ± 2.69	10.79 ± 1.79	1.45 ± 0.28
ROI 2	72.99 ± 3.6	6.91 ± 0.9	11.14 ± 1.92	7.86 ± 1.39	1.1 ± 0.24
ROI 3	85.05 ± 2.16	12.73 ± 1.83	1.77 ± 0.34	0.33 ± 0.07	0.12 ± 0.02

An ADF image of area A (see Figure 6a) is presented in Figure 7a. Three different phases are evident: a brighter one, a darker one, and a darker one with striations (indicated with dotted lines). A section of each phase (area A-1, A-2, and A-3) is selected for FFT analysis. From the FFTs of the three phases referenced in Figure 7b–d, the phases are determined to be α, β, and the B19. The B19 is identified by additional reflections to the β, which are assigned to the lattice planes $(0\bar{1}0)$ and (001) [31]. The corresponding lattice planes for each phase are indicated and the zone axes are $[2\bar{1}\bar{1}3]$, [111], and [100], respectively.

Figure 8a is a magnified ADF of area B in Figure 6a, showing a brighter and a darker phase. For each phase, areas B-1 and B-2 are selected for FFT analysis. From the FFTs of

areas B-1 and B-2, α and β are determined. The referring lattice planes are given in the FFTs. The zone axes are [$2\overline{1}\overline{1}3$] and [111], respectively.

3.7. Thermodynamic Calculation

The phase composition of Ti-6Al-4V–3Cr was calculated for 20 °C with and without Fe impurities (Fe), based on the results of the chemical analysis of the specimen. Only the proportion of hcp (α), bcc (β), and the ordered bcc (B2) were considered for the calculation, as an α + β microstructure is regarded to be the equilibrium for Ti-6Al-4V [32]. Contrary to Ti-6Al-4V–3Cr, in the Fe-containing system, a bcc and a B2 structure with the composition of TiFe was calculated. Table 6 shows the results of the calculations.

Table 6. Calculated phase composition of Ti-6Al-4V–3Cr with and without Fe impurity (Fe).

	Calculated Phase Composition (wt%)		
	α	**β**	**B2 (TiFe)**
Ti-6Al-4V–3Cr	94.13	5.87	
Ti-6Al-4V–3Cr (Fe)	93.81	5.87	0.32

3.8. Mechanical Properties

The hardness of the material is 402 ± 18 HV_{10}. Table 7 gives the mechanical properties obtained from the tensile tests, with the ultimate tensile strength (UTS), the stress at 0.2% plastic deformation ($R_{p0.2}$), the uniform elongation (A_u), and the elongation at break (A). Tensile curves of the material are shown in Figure 9.

Table 7. Mean mechanical properties of Ti-6Al-4V–3Cr for N = 4 specimens.

	$R_{p0.2}$ (MPa)	**UTS (MPa)**	**A_u (%)**	**A (%)**
Ti-6Al-4V–3Cr	1359 ± 23	1450 ± 22	1.7 ± 0.1	4.5 ± 0.2

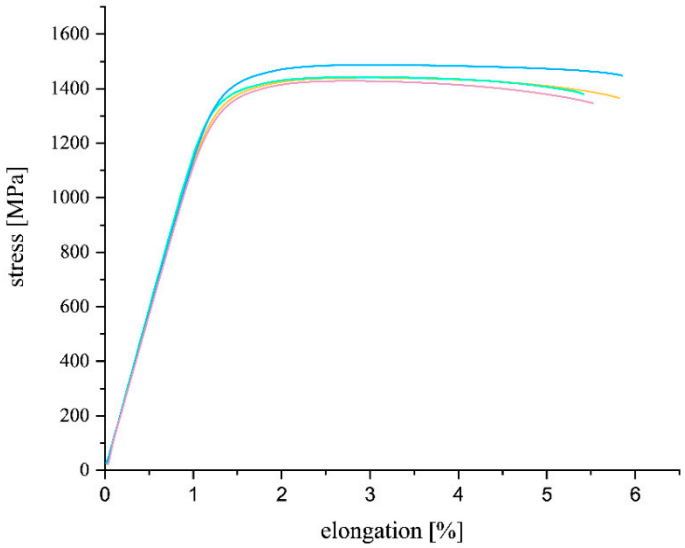


Figure 9. Tensile curves for Ti-6Al-4V–3Cr for N = 4 specimens in the as-built state and horizontal orientation. For clarity, different colors were chosen.

In Figure 10, the UTS and A of Ti-6Al-4V–3Cr are compared with the literature values of Ti-6Al-4V produced by LPBF [3,6,32–37]. For comparability with this work, the specimen orientation in these studies was identical the same as in the present investigation (horizontal). Although A of Ti-6Al-4V–3Cr is rather low, the UTS is notably higher compared to Ti-6Al-4V fabricated in LPBF.

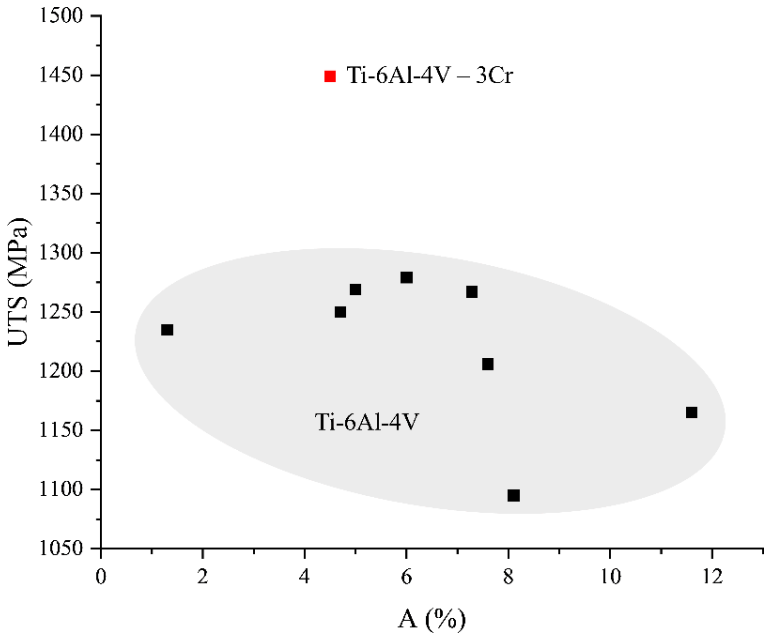


Figure 10. UTS and A for Ti-6Al-4V–3Cr compared to literature values for Ti-6Al-4V [3,6,32–37].

4. Discussion

4.1. Processability

According to the Carr index of 0.15 and the Hausner ratio of 1.17, the flowability of the powder blend is sufficient to ensure a stable powder deposition during the LPBF process. Commonly, a Carr index < 0.15 and a Hausner ratio < 1.18 are considered as an indicator for a suitable powder flowability [38].

Parts show an RD of 99.14 ± 0.11% with the voids being spherical keyhole pores and aspherical lack of fusion pores with a size < 25 µm. It should be noted that the RD refers to the TD based on thermodynamic calculations of a homogeneous alloy under equilibrium conditions. It is reasonable to assume that the phase composition and phase contents in the alloy produced in this work will differ due to the chemical inhomogeneity and rapid cooling caused by the in situ LPBF alloying. As a result, the actual TD is expected to be slightly different and the RD values must be considered with this restriction.

Generally, keyhole pores form if excessive energy is used for melting [39]. This leads to excessive evaporation, fluid dynamic instabilities, and the formation of gas bubbles. These bubbles are trapped as spherical gas pores at the approaching solid/liquid interface [40]. Excessive vaporization and increased abundance of spherical pores is also more likely when pure Cr powder is in situ alloyed with Ti-6Al-4V. Ti has a melting temperature of 1668 °C and a boiling temperature of 3287 °C, while Cr has a melting temperature of 1907 °C but a boiling temperature of only 2671 °C. In LPBF, the maximum temperature reached is assumed to be close to the boiling point of the material [41], and with Ti as the bulk material, vaporization of Cr is likely to occur. This assumption is supported by the difference between the Cr content in the feedstock material and in the specimen, as determined by chemical analysis. The powder mixture was prepared with 3 wt% Cr, while the sample contains only 1.86 wt% Cr. The simultaneous appearance of keyhole and lack of fusion pores indicates the difficulty in finding parameters for defect-free production of Ti-6Al-4V–3Cr parts, which is a common problem in LPBF in situ alloying [13]. Generally, in contrast to keyhole porosity caused by excessive energy input, occurring lack of fusion pores indicates that the energy input is too low to completely melt the powder bed [39]. Thus, it is concluded that in this study a rather low laser energy input was used to counteract the excessive gas pore formation caused by Cr in order to minimize the total pore volume. However, this is associated with the occurrence of lack of fusion pores.

4.2. Microstructure

The XRD results suggest an in situ martensite decomposition. The comparison of the phase composition between the top layer, which represents the material immediately after solidification, and the cross section reflects the microstructural evolution during the process. In the diffractogram of the top layer, α′ was identified on the basis of the lattice parameter ratio c/a = 1.587 [3], which indicates the initial transformation of primary β→α′. The presence of β in the top layer is attributed to its stabilization from the melt by sufficiently Cr-rich inclusions, which are clearly visible in the SEM, recorded simultaneously with the EBSD phase map. The XRD measurement of the cross section, which represents the entire material produced, shows it to be non-martensitic. This is supported by the lattice parameter ratio c/a = 1.597 for α [3]. The β exhibits a more pronounced peak compared to the top layer, suggesting a higher mass fraction. This supports the assumption of α′→α + β during the buildup. The in situ martensite decomposition can be explained by the application of 500 °C substrate plate preheating combined with the additional energy input from the cyclic reheating that occurs in the LPBF [9]. The influence of substrate plate preheating on martensite decomposition was described by Lei-Lei Xing et al. [42], who reported the onset of α′→α + β at 400 °C. This is due to an estimated martensite start temperature (T_M) of 650 °C for Ti-6Al-4V in the LPBF process [43], assuming initial martensitic transformation and subsequent diffusive decomposition. A similar behavior is expected for Ti-6Al-4V–3Cr when a substrate preheating of 500 °C is applied, although the T_M may differ slightly due to the presence of Cr [44]. Additional thermal input promoting martensite decomposition results from repetitive reheating during the process [45,46]. As the top layer of the material is melted, the layers underneath are heat treated by heat dissipation [47]. In addition to α and β, a low intensity peak found in the diffractogram of the top layer and the bulk material belongs to the B19 structure, which is also found in the STEM measurements.

SEM measurements show that on a macroscopic scale, LPBF in situ alloying has resulted in a chemically inhomogeneous material with varying Cr content. At higher magnification, fine lamellae corresponding to α in a brighter matrix are observed. The brighter matrix, containing higher amounts of Cr, V, and Fe, consists mainly of β. The formation of the observed continuous αGB is assumed to occur due to the thermal influence described above: the application of substrate plate preheating and cyclic reheating. In general, αGB forms during diffusional phase transformation from β⟶α [48]. However, in LPBF manufactured Ti-6Al-4V, an αGB can also develop from diffusion in sub-β transus temperature heat treatments [32,49].

EBSD shows that the majority of the material consists of fine-grained α. The few β inclusions correlate with Cr-rich areas, suggesting that β formed directly from the melt. Cr is a β-stabilizing element, and in sufficient amounts, it is able to retain β to room temperature after quenching [24]. This is reflected in the XRD measurements of the top layer, where β was observed in addition to α′. In EBSD, the α is extremely fine grained, and needle-like grains with the typical 45° angle relative to the BD for LPBF-manufactured Ti-6Al-4V [2] are barely observed. A calculated IPF map for primary β with a larger image width was selected for texture determination. A slight $\langle 111 \rangle_\beta$ texture is revealed, as opposed to the typically observed $\langle 100 \rangle_\beta$ orientation in Ti-6Al-4V [3,6,32–37,50,51]. Although the primary β is significantly shortened in the BD, the lateral extent of the grains appears to be approximately the same as the width of the melt pool. This finding, together with the absence of the $\langle 100 \rangle_\beta$ texture, can be explained by thermal supercooling. The latter is suggested to be more applicable to LPBF than classical constitutional supercooling to achieve grain refinement, although there are parallels between the two concepts. Elements that have a constitutional supercooling effect in casting have been found to induce thermal supercooling in LPBF [52–54]. Since Cr has been reported to have a grain-refining effect on cast Ti via constitutional supercooling [29], thermal supercooling in LPBF caused by Cr may therefore be suspected. The following solidification sequence is assumed [55]: During cooling from the melt, Cr tends to accumulate in front of the solidification front owing to

solute rejection at the solid/liquid interface. Consequently, accumulating Cr ahead of the solidification front destabilizes it and reduces the solidification front velocity (R). As the solidification front lags behind, thermal undercooling occurs in front of it, resulting in an increased nucleation rate. The time gained by the decelerated solidification front allows the critical nucleus size to be exceeded and the growth of randomly oriented crystallization nuclei, which can inhibit epitaxial grain growth [56]. As a result, the grain size of primary β in the longitudinal direction is significantly reduced and the formation of a strong $\langle 100 \rangle_\beta$ texture is hindered. A strong $\langle 100 \rangle_\beta$ texture can be considered a disadvantage because it results in anisotropic mechanical properties [57–60]. Although the primary β is not retained in the LPBF, it undergoes a martensitic transformation after BOR, resulting in an anisotropic microstructure. This transformation allows the formation of twelve variants for α′, which generally result in only a weak crystallographic texture. However, due to the grain growth of α′ along the $\{334\}_\beta$ and $\{344\}_\beta$ habit planes of the primary β, the inclination of the α′ needles at 45° to the primary β grain boundaries corresponding to the BD is observed, causing the anisotropy [53]. The avoidance of an excessive $\langle 100 \rangle_\beta$ texture of primary β, induced by Cr addition, can be considered as more favorable in terms of mechanical properties, as it is associated with a more isotropic orientation of α. However, only one building orientation was analyzed for tensile properties.

STEM analysis revealed the presence of lamellar α embedded in a matrix enriched in Cr, V, and Fe. The matrix consists predominantly of β, and at higher concentrations of Cr, V, and Fe, it also contains the B19 phase. An indication of B19 can also be found in XRD with a low intensity peak. The B19 phase is usually found in shape memory alloys as an intermediate phase in the B2⟶B19⟶B19′ martensite transition [31,61–64], but it can also be found in Ti-Al and doped Ti-Al systems [65–68]. With the prediction of B2 by thermodynamic calculations for Ti-6Al-4V–3Cr including Fe impurities, an ordering mechanism from β⟶B2 and a subsequent phase transformation from B2⟶B19 is proposed, with the B2 showing the composition of TiFe. In contrast, excluding Fe impurities, only α and β were predicted. Thus, the occurrence of B19 is supposed to occur due to Fe impurities.

Neither the eutectoid reaction of $\beta \longrightarrow \alpha + C15$ nor the ω were observed. No evidence was found by EBSD, XRD, and STEM measurements.

4.3. Mechanical Properties

The Ti-6Al-4V–3Cr alloy has a hardness of 402 ± 18 HV_{10}, which is comparable to the values reported in the literature for Ti-6Al-4V in LPBF [6,34,69]. The $R_{p0.2}$ of 1359 ± 23 and the UTS of 1450 ± 22 MPa are significantly higher than those determined for as-built Ti-6Al-4V in the same specimen orientation [3,6,33–37]. The high UTS and $R_{p0.2}$ are attributed to the high amount of fine-grained α, according to the Hall–Petch relationship. In addition, Zhao et al. [70] calculated a large strengthening coefficient for Cr in the β, as for other eutectoid β-stabilizers. However, the A of Ti-6Al-4V–3Cr is lower than most of the values reported for of Ti-6Al-4V produced by LPBF in the same specimen orientation [3,6,33–37,50]. The reduced ductility of Ti-6Al-4V–3Cr is thought to be due in part to the porosity of the material. Porosity is known to have a negative effect on elongation, with lack of fusion pores having a greater effect than keyhole pores [39]. The influence of the latter on ductility is attributed to higher stress concentration points [71]. In addition, αGB induces intercrystalline fracture and reduces elongation [72,73]. Furthermore, it is suspected that the B19 phase, which is described as having a more brittle character in the ab initio calculation by Wen et al. [74], has a negative effect on ductility. A more precise statement on the correlation between the B19 phase and the mechanical properties is currently not possible due to a lack of sufficient studies.

5. Conclusions

In this work, the effect of adding 3 wt% Cr to Ti-6Al-4V by LPBF in situ alloying was investigated. Processability, microstructural characteristics, and related mechanical properties were studied. The main results are summarized as follows:

(1) With LPBF in situ alloying 3 wt% Cr to Ti-6Al-4V, crack-free specimens with an RD of 99.14 ± 0.11% were produced. The addition of Cr was found to be effective in modifying microstructural and mechanical properties of Ti-6Al-4V.
(2) In situ martensite decomposition was observed. Initially, primary β was transformed into α′. The preheating of the substrate plate to 500 °C and the reheating of the lower layers during LPBF allowed the thermally driven diffusion reaction of $\alpha' \longrightarrow \alpha + \beta$ to take place.
(3) The addition of Cr resulted in thermal supercooling during solidification and induced the reduction of columnar grain growth. The grain size of primary β in the BD was significantly decreased. Thermal supercooling also results in the breakdown of the $\langle 100 \rangle_{\beta}$ texture typical of Ti-6Al-4V. This microstructure might result in more isotropic mechanical properties.
(4) The presence of the B19 phase was confirmed. It is proposed that B19 is the transformation product of the former B2, as predicted by thermodynamic calculations considering the Fe impurities present in the material.
(5) The $R_{p0.2}$, the UTS, and A were 1359 ± 23 MPa, 1450 ± 22 MPa, and 4.5 ± 0.2%, respectively. The $R_{p0.2}$ and the UTS are higher, but A is in the same range as the values for Ti-6Al-4V produced by LPBF.

The results presented in this study indicate that Cr is an interesting additive for the development of high-strength Ti alloys for various industrial applications. Nevertheless, future studies would benefit from working with pre-alloyed powders instead of in situ alloying to obtain homogeneous microstructures and reliable mechanical properties. Determining the mechanical properties in various orientations relative to the BD would be of significant interest for investigating the presumed more isotropic behavior. The addition of different Cr contents to Ti-6Al-4V and the specific study of the B19 phase is considered an interesting topic for further research as well.

Author Contributions: Conceptualization, V.S.G.; data curation, V.S.G., L.W., I.L.-P., S.M. and D.S.; funding acquisition, G.L.; investigation, V.S.G., L.W., I.L.-P., S.M. and D.S.; methodology, V.S.G.; project administration, V.S.G. and G.L.; supervision, G.L., L.K. and J.B.; visualization, V.S.G., writing—original draft, V.S.G.; writing—review and editing, G.L., J.B. and L.K. All authors have read and agreed to the published version of the manuscript.

Funding: This project is funded by the Austrian Federal Ministry for Climate Protection, Environment, Energy, Mobility, Innovation, and Technology (BMK) and is part of the "Production of the Future" program. The Grant Number of the project is 877454.

Data Availability Statement: The raw data supporting the conclusions of this article will be made available by the authors on request.

Acknowledgments: The authors would like to sincerely acknowledge the support of Pankl Racing Systems AG and Dipl. Ing. Tanja Pfeifer for supporting this research.

Conflicts of Interest: Author David Schimbäck was employed by the company Airbus Central R & T, Airbus Defence and Space GmbH. The remaining authors declare no conflicts of interest. The sponsors had no role in the design, execution, interpretation, or writing of the study.

References

1. Mair, P.; Goettgens, V.S.; Rainer, T.; Weinberger, N.; Letofsky-Papst, I.; Mitsche, S.; Leichtfried, G. Laser powder bed fusion of nano-CaB6 decorated 2024 aluminum alloy. *J. Alloys Compd.* **2021**, *863*, 158714. [CrossRef]
2. Yang, J.; Yu, H.; Yin, J.; Gao, M.; Wang, Z.; Zeng, X. Formation and control of martensite in Ti-6Al-4V alloy produced by selective laser melting. *Mater. Des.* **2016**, *108*, 308–318. [CrossRef]
3. Xu, W.; Lui, E.W.; Pateras, A.; Qian, M.; Brandt, M. In situ tailoring microstructure in additively manufactured Ti-6Al-4V for superior mechanical performance. *Acta Mater.* **2017**, *125*, 390–400. [CrossRef]
4. Simonelli, M.; Tse, Y.Y.; Tuck, C. On the texture formation of selective laser melted Ti-6Al-4V. *Metall. Mater. Trans. A Phys. Metall. Mater. Sci.* **2014**, *45*, 2863–2872. [CrossRef]
5. Xu, Y.; Zhang, D.; Guo, Y.; Hu, S.; Wu, X.; Jiang, Y. Microstructural tailoring of As-Selective Laser Melted Ti6Al4V alloy for high mechanical properties. *J. Alloys Compd.* **2020**, *816*, 152536. [CrossRef]

6. He, J.; Li, D.; Jiang, W.; Ke, L.; Qin, G.; Ye, Y.; Qin, Q.; Qiu, D. The Martensitic Transformation and Mechanical Properties of Ti6Al4V Prepared via Selective Laser Melting. *Materials* **2019**, *12*, 321. [CrossRef]
7. Cao, S.; Chu, R.; Zhou, X.; Yang, K.; Jia, Q.; Lim, C.V.S.; Huang, A.; Wu, X. Role of martensite decomposition in tensile properties of selective laser melted Ti-6Al-4V. *J. Alloys Compd.* **2018**, *744*, 357–363. [CrossRef]
8. Kumar, P.; Ramamurty, U. Microstructural optimization through heat treatment for enhancing the fracture toughness and fatigue crack growth resistance of selective laser melted Ti–6Al–4V alloy. *Acta Mater.* **2019**, *169*, 45–59. [CrossRef]
9. Zafari, A.; Barati, M.R.; Xia, K. Controlling martensitic decomposition during selective laser melting to achieve best ductility in high strength Ti-6Al-4V. *Mater. Sci. Eng. A* **2019**, *744*, 445–455. [CrossRef]
10. Mosallanejad, M.H.; Niroumand, B.; Aversa, A.; Saboori, A. In-situ alloying in laser-based additive manufacturing processes: A critical review. *J. Alloys Compd.* **2021**, *872*, 159567. [CrossRef]
11. Nagase, T.; Hori, T.; Todai, M.; Sun, S.H.; Nakano, T. Additive manufacturing of dense components in beta-titanium alloys with crystallographic texture from a mixture of pure metallic element powders. *Mater. Des.* **2019**, *173*, 107771. [CrossRef]
12. Wang, J.; Liu, Y.; Rabadia, C.D.; Liang, S.X.; Sercombe, T.B.; Zhang, L.C. Microstructural homogeneity and mechanical behavior of a selective laser melted Ti-35Nb alloy produced from an elemental powder mixture. *J. Mater. Sci. Technol.* **2021**, *61*, 221–233. [CrossRef]
13. Huang, S.; Narayan, R.L.; Tan, J.H.K.; Sing, S.L.; Yeong, W.Y. Resolving the porosity-unmelted inclusion dilemma during in-situ alloying of Ti34Nb via laser powder bed fusion. *Acta Mater.* **2021**, *204*, 116522. [CrossRef]
14. Zhang, X.; Ye, W.; Mushongera, L.; Liao, Y. Unravelling heterogeneities in sub-grain cellular structure and micromechanical response of additive manufactured Ti-Nb alloys. *Addit. Manuf.* **2022**, *59*, 103146. [CrossRef]
15. Chmielewska, A.; Wysocki, B.; Buhagiar, J.; Michalski, B.; Adamczyk-Cieślak, B.; Gloc, M.; Święszkowski, W. In situ alloying of NiTi: Influence of laser powder bed fusion (LBPF) scanning strategy on chemical composition. *Mater. Today Commun.* **2022**, *30*, 103007. [CrossRef]
16. Chlebus, E.; Kuźnicka, B.; Dziedzic, R.; Kurzynowski, T. Titanium alloyed with rhenium by selective laser melting. *Mater. Sci. Eng. A* **2015**, *620*, 155–163. [CrossRef]
17. Gussone, J.; Bugelnig, K.; Barriobero-Vila, P.; da Silva, J.C.; Hecht, U.; Dresbach, C.; Sket, F.; Cloetens, P.; Stark, A.; Schell, N.; et al. Ultrafine eutectic Ti-Fe-based alloys processed by additive manufacturing—A new candidate for high temperature applications. *Appl. Mater. Today* **2020**, *20*, 100767. [CrossRef]
18. Vilardell, A.M.; Yadroitsev, I.; Yadroitsava, I.; Albu, M.; Takata, N.; Kobashi, M.; Krakhmalev, P.; Kouprianoff, D.; Kothleitner, G.; du Plessis, A. Manufacturing and characterization of in-situ alloyed Ti6Al4V(ELI)-3 at.% Cu by laser powder bed fusion. *Addit. Manuf.* **2020**, *36*, 101436. [CrossRef]
19. Krakhmalev, P.; Yadroitsev, I.; Yadroitsava, I.; de Smidt, O. Functionalization of biomedical Ti6Al4V via in situ alloying by Cu during laser powder bed fusion manufacturing. *Materials* **2017**, *10*, 1154. [CrossRef]
20. Guo, S.; Lu, Y.; Wu, S.; Liu, L.; He, M.; Zhao, C.; Gan, Y.; Lin, J.; Luo, J.; Xu, X.; et al. Preliminary study on the corrosion resistance, antibacterial activity and cytotoxicity of selective-laser-melted Ti6Al4V-xCu alloys. *Mater. Sci. Eng. C* **2017**, *72*, 631–640. [CrossRef]
21. Vrancken, B.; Thijs, L.; Kruth, J.P.; Van Humbeeck, J. Microstructure and mechanical properties of a novel β titanium metallic composite by selective laser melting. *Acta Mater.* **2014**, *68*, 150–158. [CrossRef]
22. Zhang, T.; Huang, Z.; Yang, T.; Kong, H.; Luan, J.; Wang, A.; Wang, D.; Kuo, W.; Wang, Y.; Liu, C.-T. In situ design of advanced titanium alloy with concentration modulations by additive manufacturing. *Science* **2021**, *374*, 478–482. [CrossRef] [PubMed]
23. Goettgens, V.S.; Kaserer, L.; Braun, J.; Letofsky-Papst, I.; Mitsche, S.; Leichtfried, G. Microstructure of a modulated Ti-6Al-4V—Cu alloy fabricated via in situ alloying in laser powder bed fusion. *Materialia* **2023**, *28*, 101731. [CrossRef]
24. Kolli, R.P.; Devaraj, A. A review of metastable beta titanium alloys. *Metals* **2018**, *8*, 506. [CrossRef]
25. Hayat, M.A.; Suliman, S.M.A. An economical heat treatment cycle for IMI Ti-230. *Mater. Manuf. Process.* **1998**, *13*, 203–212. [CrossRef]
26. Donachie, M.J. *Titanium—A Techincal Guide*; ASM International: Almere, The Netherlands, 2000; Volume 99. [CrossRef]
27. Ho, W.F.; Chiang, T.Y.; Wu, S.C.; Hsu, H.C. Mechanical properties and deformation behavior of cast binary Ti-Cr alloys. *J. Alloys Compd.* **2009**, *468*, 533–538. [CrossRef]
28. Hsu, H.C.; Wu, S.C.; Chiang, T.Y.; Ho, W.F. Structure and grindability of dental Ti-Cr alloys. *J. Alloys Compd.* **2009**, *476*, 817–825. [CrossRef]
29. Bermingham, M.J.; McDonald, S.D.; StJohn, D.H.; Dargusch, M.S. Segregation and grain refinement in cast titanium alloys. *J. Mater. Res.* **2009**, *24*, 1529–1535. [CrossRef]
30. Andersson, J.O.; Helander, T.; Höglund, L.; Shi, P.; Sundman, B. Thermo-Calc & DICTRA, computational tools for materials science. *Calphad Comput. Coupling Phase Diagr. Thermochem.* **2002**, *26*, 273–312. [CrossRef]
31. Fukuda, T.; Saburi, T.; Chihara, T.; Tsuzuki, Y. Mechanism of B2-B19-B19′ Transformation in Shape Memory Ti-Ni-Cu Alloys. *Mater. Trans. JIM* **1995**, *36*, 1244–1248. [CrossRef]
32. Vrancken, B.; Thijs, L.; Kruth, J.P.; Van Humbeeck, J. Heat treatment of Ti6Al4V produced by Selective Laser Melting: Microstructure and mechanical properties. *J. Alloys Compd.* **2012**, *541*, 177–185. [CrossRef]
33. Cain, V.; Thijs, L.; Van Humbeeck, J.; Van Hooreweder, B.; Knutsen, R. Crack propagation and fracture toughness of Ti6Al4V alloy produced by selective laser melting. *Addit. Manuf.* **2015**, *5*, 68–76. [CrossRef]

34. Rafi, H.K.; Karthik, N.V.; Gong, H.; Starr, T.L.; Stucker, B.E. Microstructures and mechanical properties of Ti6Al4V parts fabricated by selective laser melting and electron beam melting. *J. Mater. Eng. Perform.* **2013**, *22*, 3872–3883. [CrossRef]
35. Facchini, L.; Magalini, E.; Robotti, P.; Molinari, A.; Höges, S.; Wissenbach, K. Ductility of a Ti-6Al-4V alloy produced by selective laser melting of prealloyed powders. *Rapid Prototyp. J.* **2010**, *16*, 450–459. [CrossRef]
36. Vilaro, T.; Colin, C.; Bartout, J.D. As-fabricated and heat-treated microstructures of the Ti-6Al-4V alloy processed by selective laser melting. *Metall. Mater. Trans. A Phys. Metall. Mater. Sci.* **2011**, *42*, 3190–3199. [CrossRef]
37. Zhang, D.; Wang, L.; Zhang, H.; Maldar, A.; Zhu, G.; Chen, W.; Park, J.-S.; Wang, J.; Zeng, X. Effect of heat treatment on the tensile behavior of selective laser melted Ti-6Al-4V by in situ X-ray characterization. *Acta Mater.* **2020**, *189*, 93–104. [CrossRef]
38. Hao, T. Understanding empirical powder flowability criteria scaled by Hausner ratio or Carr index with the analogous viscosity concept. *RSC Adv.* **2015**, *5*, 57212–57215. [CrossRef]
39. Montalbano, T.; Briggs, B.N.; Waterman, J.L.; Nimer, S.; Peitsch, C.; Sopcisak, J.; Trigg, D.; Storck, S. Uncovering the coupled impact of defect morphology and microstructure on the tensile behavior of Ti-6Al-4V fabricated via laser powder bed fusion. *J. Mater. Process. Technol.* **2021**, *294*, 117113. [CrossRef]
40. Dilip, J.J.S.; Zhang, S.; Teng, C.; Zeng, K.; Robinson, C.; Pal, D.; Stucker, B. Influence of processing parameters on the evolution of melt pool, porosity, and microstructures in Ti-6Al-4V alloy parts fabricated by selective laser melting. *Prog. Addit. Manuf.* **2017**, *2*, 157–167. [CrossRef]
41. Karayagiz, K.; Elwany, A.; Tapia, G.; Franco, B.; Johnson, L.; Ma, J.; Karaman, I.; Arróyave, R. Numerical and experimental analysis of heat distribution in the laser powder bed fusion of Ti-6Al-4V. *IISE Trans.* **2019**, *51*, 136–152. [CrossRef]
42. Xing, L.L.; Zhang, W.J.; Zhao, C.C.; Gao, W.Q.; Shen, Z.J.; Liu, W. Influence of powder bed temperature on the microstructure and mechanical properties of ti-6al-4v alloys fabricated via laser powder bed fusion. *Materials* **2021**, *14*, 2278. [CrossRef] [PubMed]
43. Kenel, C.; Grolimund, D.; Li, X.; Panepucci, E.; Samson, V.A.; Sanchez, D.F.; Marone, F.; Leinenbach, C. In situ investigation of phase transformations in Ti-6Al-4V under additive manufacturing conditions combining laser melting and high-speed micro-X-ray diffraction. *Sci. Rep.* **2017**, *7*, 16358. [CrossRef] [PubMed]
44. Neelakantan, S.; Rivera-Díaz-del-Castillo, P.E.J.; van der Zwaag, S. Prediction of the martensite start temperature for β titanium alloys as a function of composition. *Scr. Mater.* **2009**, *60*, 611–614. [CrossRef]
45. Pantawane, M.V.; Dasari, S.; Mantri, S.A.; Banerjee, R.; Dahotre, N.B. Rapid thermokinetics driven nanoscale vanadium clustering within martensite laths in laser powder bed fused additively manufactured Ti6Al4V. *Mater. Res. Lett.* **2020**, *8*, 383–389. [CrossRef]
46. Pantawane, M.V.; Ho, Y.H.; Joshi, S.S.; Dahotre, N.B. Computational Assessment of Thermokinetics and Associated Microstructural Evolution in Laser Powder Bed Fusion Manufacturing of Ti6Al4V Alloy. *Sci. Rep.* **2020**, *10*, 7579. [CrossRef]
47. Goettgens, V.S.; Kaserer, L.; Braun, J.; Busch, R.; Berthold, L.; Patzig, C.; Leichtfried, G. Microstructural evolution and mechanical properties of Ti-6Al-4V in situ alloyed with 3.5 wt.% Cu by laser powder bed fusion. *Materialia* **2023**, *32*, 101928. [CrossRef]
48. Gao, X.; Zhang, S.; Wang, L.; Yang, K.; Wang, P.; Chen, H. Evolution of grain boundary α phase during cooling from β phase field in a α + β titanium alloy. *Mater. Lett.* **2021**, *301*, 130318. [CrossRef]
49. Liu, J.; Zhang, K.; Yang, Y.; Wang, H.; Zhu, Y.; Huang, A. Grain boundary α-phase precipitation and coarsening: Comparing laser powder bed fusion with as-cast Ti-6Al-4V. *Scr. Mater.* **2022**, *207*, 114261. [CrossRef]
50. Xu, W.; Brandt, M.; Sun, S.; Elambasseril, J.; Liu, Q.; Latham, K.; Xia, K.; Qian, M. Additive manufacturing of strong and ductile Ti-6Al-4V by selective laser melting via in situ martensite decomposition. *Acta Mater.* **2015**, *85*, 74–84. [CrossRef]
51. Wu, M.W.; Chen, J.K.; Tsai, M.K.; Wang, S.H.; Lai, P.H. Intensification of preferred orientation in the additive manufactured Ti-6Al-4V alloy after heat treatment. *Mater. Lett.* **2021**, *286*, 129198. [CrossRef]
52. Tan, Q.; Yin, Y.; Prasad, A.; Li, G.; Zhu, Q.; StJohn, D.H.; Zhang, M.-X. Demonstrating the roles of solute and nucleant in grain refinement of additively manufactured aluminium alloys. *Addit. Manuf.* **2022**, *49*, 102516. [CrossRef]
53. Bermingham, M.; StJohn, D.; Easton, M.; Yuan, L.; Dargusch, M. Revealing the Mechanisms of Grain Nucleation and Formation During Additive Manufacturing. *JOM* **2020**, *72*, 1065–1073. [CrossRef]
54. Bermingham, M.J.; StJohn, D.H.; Krynen, J.; Tedman-Jones, S.; Dargusch, M.S. Promoting the columnar to equiaxed transition and grain refinement of titanium alloys during additive manufacturing. *Acta Mater.* **2019**, *168*, 261–274. [CrossRef]
55. Braun, J.; Kaserer, L.; Stajkovic, J.; Kestler, H.; Leichtfried, G. Grain refinement mechanisms of alloying molybdenum with carbon manufactured by laser powder bed fusion. *Mater. Des.* **2022**, *215*, 110507. [CrossRef]
56. Rappaz, M.; David, S.A.; Vitek, J.M.; Boatner, L.A. Development of microstructures in Fe-15Ni-15Cr single crystal electron beam welds. *Metall. Trans. A* **1989**, *20*, 1125–1138. [CrossRef]
57. Wilson-Heid, A.E.; Wang, Z.; McCornac, B.; Beese, A.M. Quantitative relationship between anisotropic strain to failure and grain morphology in additively manufactured Ti-6Al-4V. *Mater. Sci. Eng. A* **2017**, *706*, 287–294. [CrossRef]
58. He, Y.; Ma, Y.; Zhang, W.; Wang, Z. Anisotropic tensile and fatigue properties of laser powder bed fusion Ti6Al4V under high temperature. *Eng. Fract. Mech.* **2022**, *276*, 108948. [CrossRef]
59. Pantawane, M.V.; Yang, T.; Jin, Y.; Joshi, S.S.; Dasari, S.; Sharma, A.; Krokhin, A.; Srinivasan, S.G.; Banerjee, R.; Neogi, A.; et al. Crystallographic texture dependent bulk anisotropic elastic response of additively manufactured Ti6Al4V. *Sci. Rep.* **2021**, *11*, 633. [CrossRef] [PubMed]
60. Simonelli, M.; Tse, Y.Y.; Tuck, C. Effect of the build orientation on the mechanical properties and fracture modes of SLM Ti-6Al-4V. *Mater. Sci. Eng. A* **2014**, *616*, 1–11. [CrossRef]
61. Sewak, R.; Dey, C.C. Martensitic phase transformation in TiNi. *Sci. Rep.* **2019**, *9*, 13500. [CrossRef]

62. Otsuka, K.; Ren, X. Physical metallurgy of Ti-Ni-based shape memory alloys. *Prog. Mater. Sci.* **2005**, *50*, 511–678. [CrossRef]
63. Tadaki, T.; Wayman, C.M. Electron microscopy studies of martensitic transformations in $Ti_{50}Ni_{50-x}Cu_x$ alloys. Part II. Morphology and crystal structure of martensites. *Metallography* **1982**, *15*, 247–258. [CrossRef]
64. Miyamoto, H.; Taniwaki, T.; Ohba, T.; Otsuka, K.; Nishigori, S.; Kato, K. Two-stage B2-B19-B19′ martensitic transformation in a $Ti_{50}Ni_{30}Cu_{20}$ alloy observed by synchrotron radiation. *Scr. Mater.* **2005**, *53*, 171–175. [CrossRef]
65. Abe, E.; Kumagai, T.; Nakamura, M. New ordered structure of TiAl studied by high-resolution electron microscopy. *Intermetallics* **1996**, *4*, 327–333. [CrossRef]
66. Schmoelzer, T.; Stark, A.; Schwaighofer, E.; Lippman, T.; Mayer, S.; Clemens, H. In Situ Synchrotron Study of B19 Phase Formation in an Intermetallic γ-TiAl Alloy.pdf. *Adv. Eng. Mater.* **2012**, *14*, 445–448. [CrossRef]
67. Song, L.; Xu, X.J.; You, L.; Liang, Y.F.; Lin, J.P. B19 phase in Ti-45Al-8.5Nb-0.2W-0.2B-0.02Y alloy. *J. Alloys Compd.* **2015**, *618*, 305–310. [CrossRef]
68. Ducher, R.; Viguier, B.; Lacaze, J. Modification of the crystallographic structure of γ-TiAl alloyed with iron. *Scr. Mater.* **2002**, *47*, 307–313. [CrossRef]
69. Li, H.; Jia, D.; Yang, Z.; Liao, X.; Jin, H.; Cai, D.; Zhou, Y. Effect of heat treatment on microstructure evolution and mechanical properties of selective laser melted Ti–6Al–4V and TiB/Ti–6Al–4V composite: A comparative study. *Mater. Sci. Eng. A* **2021**, *801*, 140415. [CrossRef]
70. Zhao, G.H.; Liang, X.Z.; Kim, B.; Rivera-Díaz-del-Castillo, P.E.J. Modelling strengthening mechanisms in beta-type Ti alloys. *Mater. Sci. Eng. A* **2019**, *756*, 156–160. [CrossRef]
71. Kan, W.H.; Gao, M.; Zhang, X.; Liang, E.; Chiu, N.S.L.; Lim, C.V.S.; Huang, A. The influence of porosity on Ti-6Al-4V parts fabricated by laser powder bed fusion in the pursuit of process efficiency. *Int. J. Adv. Manuf. Technol.* **2022**, *119*, 5417–5438. [CrossRef]
72. Liu, C.M.; Wang, H.M.; Tian, X.J.; Liu, D. Development of a pre-heat treatment for obtaining discontinuous grain boundary α in laser melting deposited Ti-5Al-5Mo-5V-1Cr-1Fe alloy. *Mater. Sci. Eng. A* **2014**, *604*, 176–182. [CrossRef]
73. Carroll, B.E.; Palmer, T.A.; Beese, A.M. Anisotropic tensile behavior of Ti-6Al-4V components fabricated with directed energy deposition additive manufacturing. *Acta Mater.* **2015**, *87*, 309–320. [CrossRef]
74. Wen, Y.; Wang, L.; Liu, H.; Song, L. Ab initio study of the elastic and mechanical properties of b19 TiAl. *Crystals* **2017**, *7*, 39. [CrossRef]

Disclaimer/Publisher's Note: The statements, opinions and data contained in all publications are solely those of the individual author(s) and contributor(s) and not of MDPI and/or the editor(s). MDPI and/or the editor(s) disclaim responsibility for any injury to people or property resulting from any ideas, methods, instructions or products referred to in the content.